Bioactive Materials 18 (2022) 421–432

Contents lists available at ScienceDirect

Bioactive Materials

journal homepage: www.keaipublishing.com/en/journals/bioactive-materials

Simultaneously enhancing the photocatalytic and photothermal effect of NH_2-MIL-125-GO-Pt ternary heterojunction for rapid therapy of bacteria-infected wounds

Yue Luo [a], Bo Li [a], Xiangmei Liu [a,b,***], Yufeng Zheng [c], Erjing Wang [a,**], Zhaoyang Li [d], Zhenduo Cui [d], Yanqin Liang [d], Shengli Zhu [d], Shuilin Wu [c,*]

[a] Biomedical Materials Engineering Research Center, Collaborative Innovation Center for Advanced Organic Chemical Materials Co-constructed By the Province and Ministry, Hubei Key Laboratory of Polymer Materials, Ministry-of-Education Key Laboratory for the Green Preparation and Application of Functional Materials, School of Materials Science & Engineering, Hubei University, Wuhan, 430062, China

[b] School of Life Science and Health Engineering, Hebei University of Technology, Tianjin, 300401, China

[c] School of Materials Science and Engineering, Peking University, Beijing, 100871, China

[d] School of Materials Science & Engineering, The Key Laboratory of Advanced Ceramics and Machining Technology By the Ministry of Education of China, Tianjin University, Tianjin, 300072, China

ARTICLE INFO

Keywords:
Bacterial infection
NH_2-MIL-125
Antibacterial
Photocatalytic
Photothermal

ABSTRACT

Infections caused by bacteria threaten human health, so how to effectively kill bacteria is an urgent problem. We therefore synthesized a NH_2-MIL-125-GO-Pt ternary composite heterojunction with graphene oxide (GO) and platinum (Pt) nanoparticles co-doped with metal-organic framework (NH_2-MIL-125) for use in photocatalytic and photothermal synergistic disinfection under white light irradiation. Due to the good conductivity of GO and the Schottky junction between Pt and MOF, the doping of GO and Pt will effectively separate and transfer the photogenerated electron-hole pairs generated by NH_2-MIL-125, thereby effectively improving the photocatalytic efficiency of NH_2-MIL-125. Meanwhile, NH_2-MIL-125-GO-Pt has good photothermal effect under white light irradiation. Therefore, the NH_2-MIL-125-GO-Pt composite can be used for effective sterilization. The antibacterial efficiency of NH_2-MIL-125-GO-Pt against *Staphylococcus aureus* and *Escherichia coli* were as high as 99.94% and 99.12%, respectively, within 20 min of white light irradiation. *In vivo* experiments showed that NH_2-MIL-125-GO-Pt could effectively kill bacteria and promote wound healing. This work brings new insights into the use of NH_2-MIL-125-based photocatalyst materials for rapid disinfection of environments with pathogenic microorganisms.

Credit author statement

Yue Luo: Conceptualization, Methodology, Writing- original draft, Data curation, Investigation. Bo Li: Methodology, Visualization. Erjing Wang, Xiangmei Liu: Conceptualization, Writing - review & editing, Supervision, Project administration. Yufeng Zheng: Methodology, Visualization. Zhaoyang Li, ZhenDuo Cui: Methodology. Yanqin Liang, Shengli Zhu: Methodology. Shuilin Wu: Conceptualization, Writing - review & editing, Supervision, Project administration, Funding acquisition.

1. Introduction

Bacterial contamination is one of the most challenging issues in many fields such as medical care, food, and the environment [1,2]. The most effective antibacterial method at present is the use of antibiotics to

Peer review under responsibility of KeAi Communications Co., Ltd.

* Corresponding author.
** Corresponding author.
*** Corresponding author. Biomedical Materials Engineering Research Center, Collaborative Innovation Center for Advanced Organic Chemical Materials Co-constructed by the Province and Ministry, Hubei Key Laboratory of Polymer Materials, Ministry-of-Education Key Laboratory for the Green Preparation and Application of Functional Materials, School of Materials Science & Engineering, Hubei University, Wuhan, 430062, China.

E-mail addresses: liuxiangmei1978@163.com (X. Liu), wangej@hubu.edu.cn (E. Wang), slwu@pku.edu.cn (S. Wu).

https://doi.org/10.1016/j.bioactmat.2022.03.035
Received 27 February 2022; Received in revised form 20 March 2022; Accepted 20 March 2022
2452-199X/

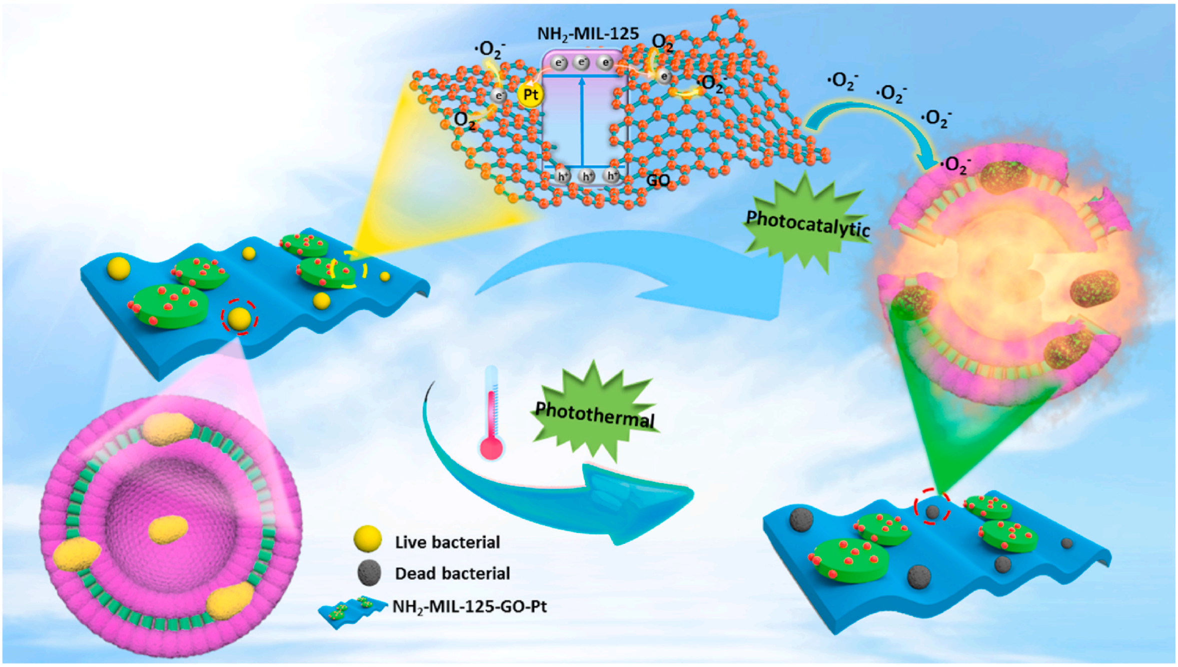

Scheme 1. Schematic diagram of synergistic killing of bacteria by photocatalysis and photothermal effect of NH_2-MIL-125-GO-Pt under visible light irradiation.

sterilize. However, with the misuse of antibiotics, pathogenic bacteria have developed resistance to almost all available conventional antibiotics [3]. According to a recent report by the World Health Organization, antimicrobial resistance will become a huge public health threat by 2050, causing 10 million deaths a year [4]. Therefore, the development of a new type of high-efficiency antibacterial to solve the problem of bacterial resistance has become a top priority. In the past few decades, nanomaterials have been able to bind and destroy bacterial cell membranes, resulting in leakage of cytoplasmic components [5]. With nanomaterials as the main body of antibacterial, various antibacterial methods have been derived. Among the many antibacterial methods, photocatalytic antibacterial is an efficient, energy-saving and universal method. The photocatalyst convert solar energy into chemical energy of redox reaction, and reacts with water and the dissolved oxygen in the water to produce various reactive oxygen species (ROS) such as hydroxyl radicals (·OH), superoxide anion ($\cdot O_2^-$), unisexual state oxygen ($^1O_2$) and so on, these ROS can effectively destroy bacteria cell membrane and the bacteria content so as to achieve an effective sterilization effect [6–8]. A large number of materials have been used for photocatalytic antibacterial research, such as CuS, Bi_2S_3, and so on [9–12]. Currently, the novel visible light driven and multicenter catalytic semiconductors being investigated by scientists are usually metal-organic frameworks (MOF).

MOF are a new kind of materials, which are composed of metal ions and organic ligands by coordination bonds [13]. Most of MOF have the photocatalytic redox ability [14]. However, the photocatalytic efficiency of pure MOFs is very low due to the wide band gap, weak absorption of visible light, and excessively fast recombination rate of photogenerated carriers in most MOFs [15]. To address the above shortcomings, the construction of heterostructures by coupling two semiconductors with appropriate band positions is an effective method to enhance the photocatalytic efficiency of MOF [16]. Because the difference of interfacial potential will generate a built-in electric field, which will induce electron and hole transfer and inhibit their recombination. In addition to constructing heterojunction with MOF, the doping of precious Pt nanoparticles is often employed for modification [17,18]. A Schottky junction is formed at the interface between the MOF and Pt nanoparticles. When the MOF is illuminated, the photogenerated electron on the CB of MOF can be transferred to the Pt. Thereby, the separation efficiency of the photogenerated carriers of the MOF is improved, and the photocatalytic performance of the MOF is finally improved.

To sum up, we took a common MOF (NH_2-MIL-125) as an example, in order to improve the photocatalytic efficiency and antibacterial efficiency of NH_2-MIL-125, we constructed the NH_2-MIL-125-GO-Pt ternary heterojunction (Scheme 1). The two-dimensional material graphene oxide (GO) and Pt nanoparticles were introduced into NH_2-MIL-125. GO as an excellent conductor would guide the photogenerated electrons generated in NH_2-MIL-125. Meanwhile, Pt nanoparticles would form a Schottky junction with NH_2-MIL-125, which would further conduct the photogenerated electrons of NH_2-MIL-125, so the doping of GO and Pt nanoparticles could effectively separate the photogenerated electron-hole pair of NH_2-MIL-125, thereby enhancing the photocatalytic efficiency of NH_2-MIL-125. Due to the improvement of photocatalytic efficiency, the yield of ROS also increased. Meanwhile, NH_2-MIL-125-GO-Pt had a good photothermal effect. Therefore, under the synergistic effect of photothermal and photocatalysis, the NH_2-MIL-125-GO-Pt composite material had a high antibacterial efficiency, and the antibacterial efficiency of NH_2-MIL-125-GO-Pt against *Staphylococcus aureus* (*S. aureus*) and *Escherichia coli* (*E. coli*) were as high as 99.94% and 99.12%, respectively.

2. Experiment method

2.1. Synthesis of NH_2-MIL-125

First, 0.56 g of 2-aminoterephthalic acid (H_2BDC-NH_2) was dispersed in a mixed solution of 32 mL of DMF and 9 mL of methanol and dissolved uniformly under magnetic stirring, and then 600 μL of titanium isopropoxide was added dropwise under stirring. The above solution was continuously stirred for 10 min, and then the above solution was transferred to a 100 mL reactor and reacted in a muffle furnace at 150 °C for 24 h. After the reactor was cooled, the material was centrifuged, washed with DMF and ethanol 3 times, and finally dried for use.

2.2. Synthesis of NH_2-MIL-125-GO

The GO powder (20 mg) was dispersed in a well-dissolved titanium isopropoxide/2-aminoterephthalic acid mixed solution. The resulting suspension was then stirred and subjected to the same synthesis procedure as NH_2-MIL-125.

2.3. Synthesis of NH_2-MIL-125-GO-Pt

First, 20 mg of NH_2-MIL-125-GO was dispersed in 10 mL of deionized water. Then 125 μL of chloroplatinic acid (40 mg/mL) solution was added to the above solution and stirred for 2 h. Then 1.25 mL of sodium borohydride aqueous solution (4 mg/mL) was added quickly to the above solution and stirred for more than 3 h. After the reaction, the sample was centrifugally and washed with deionized water and ethanol for 5 times, severally. Finally, the sample was dried.

2.4. Material characterization

Field emission scanning electron microscope (FE-SEM JSM7100F, JEOL, JP) and transmission electron microscope (TEM, Tecnai G20, FEI, USA) were used to observe the morphology and the crystal structure of the material, respectively. X-ray diffraction (XRD, D8A25, Bruker, Germany) was used to determine the material composition and phase structure. X-ray photoelectron spectroscopy (XPS, ESCALAB 250Xi, Thermo Scientific, USA) with monochromatic Al-Kα source (1486.6 eV) was used to study the elemental composition of materials. C 1s (284.8 eV) was used as the calibration peak. An ultraviolet–visible (UV–vis) spectrophotometer (UV-3600, Shimadu, JP) was used to measure the UV–vis diffuse reflectance spectrum (DRS) spectrum obtained from the sample. The light source (300 W Xe lamp, PLS-SXE300, China) was used to evaluate photocatalytic and photothermal performance of materials, and to record temperature changes of materials through a thermal imager (testo 875i, Testo Instruments International Trade (Shanghai) Co., Ltd.). Fluorescence spectrometer (LS-55, PE, USA) was used for room temperature photoluminescence (PL) measurement.

2.5. Photoelectrochemical measurement

A three-electrode CHI-660E electrochemical workstation was used to study the photoelectrochemical properties of the material. The platinum electrode was used as the counter electrode, the Ag/AgCl electrode was used as the reference electrode, and the sample group was used as the working electrode. A 300 W xenon lamp was used as the light source (0.4 W/cm^2) for photocurrent testing, electrochemical impedance spectroscopy (EIS) measurement and linear sweep voltammetry (LSV) measurement, and Na_2SO_4 solution (0.5 M) was used as the electrolyte. Among them, the working electrode was prepared by the following method. Dispersing 200 μL of 5% Nafion solution evenly in 1 mL of absolute ethanol, and then adding 3 mg of sample in the above solution, and sonicating for 20 min. The formed uniform sample suspension was dropped on the ITO glass electrode. Finally, the resulting sample film was dried overnight.

2.6. ROS test

In order to evaluate the photocatalytic performance of the synthesized samples, electron spin resonance (ESR, JES-FA200, JEOL, Japan) spectra were recorded. 5, 5-dimethyl-1-pyrrolin-N-oxide (DMPO) was used as the superoxide anion ($\cdot O_2^-$) trapping agent, and 40 μL 2.5 mg/mL NH_2-MIL-125-GO-Pt suspension and 160 μL trapping agent were irradiated under simulated sunlight. The $\cdot O_2^-$ of the samples were analyzed by ESR spectroscopy.

2.7. DFT calculation

All the self-consistent periodic DFT calculations were carried out using the DMol3 code as implemented in the Materials Studio package. The electron exchange and correlation were described with GGA-PBE functional. At the same time, the DFT-D (TS) method was used in performing the DFT calculations for the dispersion correction. The localized double-numerical quality basis set with a polarization d-function (DNP-3.5 file) was chosen to expand the wave functions. The core electrons of the metal atoms were treated using the effective core potentials (ECP), and the orbital cutoff were 4.5 Å for all atoms. For the geometry optimization, the convergences of the energy, Max. force, and Ma. displacement was set as 1×10^{-4} Ha, 2×10^{-2} Ha/Å, and 5×10^{-2} Å, and the SCF convergence for each electronic energy was set as 1.0×10^{-5} Ha.

2.8. Photothermal test

In order to evaluate the photothermal effect of the sample, the sample was placed in a 96-well plate containing 160 μL of aqueous solution and 40 μL of samples, and each well was exposed to a 300 W xenon lamp (0.4 W/cm^2) for 20 min. The temperature is recorded at 2 min intervals.

2.9. In vitro antibacterial test

The antibacterial activity of the samples against Gram-positive *Staphylococcus aureus* (*S. aureus*) (1×10^7 CFU/mL) and Gram-negative *Escherichia coli* (*E, coli*) was evaluated by plate coating method in *vitro*. 160 μL of bacterial solution and 40 μL of medium or 2.5 mg/mL of different samples (NH_2-MIL-125, NH_2-MIL-125-GO and NH_2-MIL-125-GO-Pt, NH_2-MIL-125-Pt) were placed in 96-well plates. They were then exposed to 300 W xenon light (0.4 W/cm^2) or cultured in the absence of light for 20 min. After culture under dark and light conditions, *S. aureus* and *E. coli* liquid were sucked out and diluted 100 times with sterile LB medium. Then, 20 μL of the dilution was transferred to an agar plate and cultured at 37 °C for 24 h. The bacterial colony number (A) was photographed and counted, and the antibacterial efficiency could be obtained by the following formula:

$$\text{Antibacterial ratio } (\%) = \frac{\text{Acontrol} - \text{Asample}}{\text{Acontrol}} \times 100\%$$

BCA test, BCA protein test was used to identify bacterial cell membrane damage. First of all, the five antibacterial experimental groups (Control, NH_2-MIL-125, NH_2-MIL-125-GO, NH_2-MIL-125-GO-Pt, NH_2-MIL-125-Pt) completed the antibacterial experiment according to the above antibacterial steps. These mixed solutions were then centrifuged at 10000 rpm for 5 min at 4 °C. Transferring 25 μL of the supernatant to 200 μL of BCA reagent in a 96-well plate. Finally, the microplate reader was used to measure protein leakage.

Bacterial membrane permeability measurement, O-nitrophenyl-β-galactoside (ONPG) was used to observe the change of bacterial membrane permeability on the sample surface. After treatment with or without light, the ONPG test was used to detect the absorbance of the supernatant at 420 nm.

Detection of reactive oxygen species in bacteria. The bacterial solution (0.5 mL of 10^9 CFU/mL) was centrifuged (5000 rpm for 6 min) and washed 3 times with PBS, then 100 μL of DCFH-DA diluted with PBS (1:2000) was added and incubated for 30 min at 37 °C. After that, DCFH-DA was removed and the sample solution (500 μg/mL) was added, the mixture was illuminated with white light for 20 min. Finally, the bacteria was observed through a fluorescence microscope (IX73, Olympus, USA).

Bacteria morphology detection, SEM was used to closely examine the membrane morphology of *S. aureus* and *E. coli*. After the above sterilization process, the LB medium in the sample was replaced with 2.5% glutaraldehyde and the bacteria were immobilized for 2 h, then the sample was rinsed with sterilized PBS (pH = 7.4) at least 3 times. Then the samples were dehydrated with alcohol (10%, 30%, 50%, 70%, 90% and 100%) for 15 min respectively, and then the samples were dried in a 4 °C refrigerator.

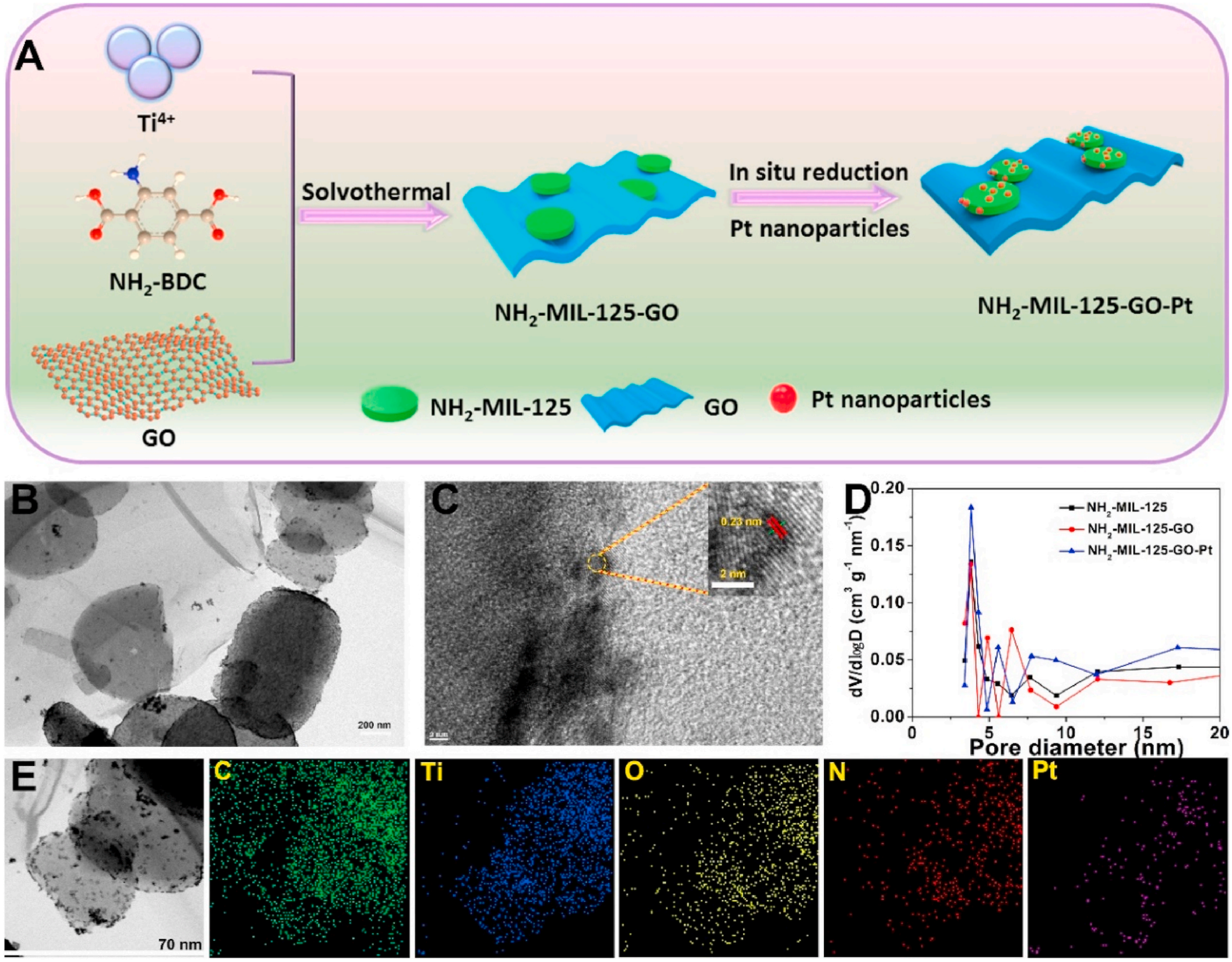

Fig. 1. (A) Schematic diagram of the synthetic route of NH_2-MIL-125-GO-Pt. (B) TEM images of NH_2-MIL-125-GO-Pt. (C) High-resolution TEM image of NH_2-MIL-125-GO-Pt and part of the enlarged image from the red circle. (D) Pore-size distribution curve of NH_2-MIL-125, NH_2-MIL-125-GO and NH_2-MIL-125-GO-Pt. (E) TEM elemental mappings of the NH_2-MIL-125-GO-Pt.

2.10. Cell viability determination

The cell viability of the sample against NIH-3T3 cells (Wuhan Tongji Hospital) was evaluated by 3-[4,5-dimethylthiazol-2-yl]-2,5-diphenyltetrazolium bromide (MTT). Adding 20 μL medium, 5 mg/mL NH_2-MIL-125, NH_2-MIL-125-GO, NH_2-MIL-125-GO-Pt, NH_2-MIL-125-Pt solution to 180 μL 1×10^4 cells/mL cells and then culturing the above solution in a 96-well plate. After culturing in a 5% CO_2 incubator at 37 °C for 1 day, the solution was taken out from each well, and 200 μL 0.5 mg/mL MTT solution was added to each well, and then cultured at 37 °C for 4 h. Next, replacing the MTT solution in each well with 200 μL dimethyl sulfoxide (DMSO) and shake for 10 min. Finally, the absorbance of DMSO at 570 nm was measured using a SpectraMax I3 Molecular device.

For the cell fluorescence staining experiments, after the material was co-cultured with the cells for 1 day, the supernatant was sucked out and the cells were fixed with 4% formaldehyde for 10 min. The cells were then stained with FITC (YiSen, Shanghai) for 30 min. After washing with PBS for 3 times, DAPI (Shanghai Yisen) was used to stain for 30 s. Finally, after washing with PBS for three times, images were taken by inverted fluorescence microscope (IFM, Olympus, IX73).

2.11. In vivo animal assay

Male BALB/c mice (weight 18–20 g) were purchased from the Animal Hospital of Huazhong Agricultural University. The animal experimental protocol was approved by the Animal Research Committee of Tongji Medical College, Huazhong University of Science and Technology, Wuhan. All experimental operations were in accordance with the regulations of the Ministry of Health of the People's Republic of China on the Administration of Animals and the Guidelines for the Care and Use of Laboratory Animals in China. All rats had good living conditions before the experiment and were divided into three groups (control group, 3M, NH_2-MIL-125-GO-Pt). Then set up three time groups (2, 5 and 10 days) with 12 mice in each group. After anesthetized with 16% chloral hydrate (30 mg/kg), a wound model was made on the back of the rat with a tool, and then 15 μL of 10^8 CFU/mL bacterial solution was mixed with 50 μL PBS (control and 3M groups) or 500 μg/mL of NH_2-MIL-125-GO-Pt (experimental group). After 20 min of white light irradiation, the wounds of the control group and the experimental group were bandaged with opaque sterile medical tape. The 3M group was covered with a standard 3M wound dressing. The rats were then placed in a suitable environment for feeding. After 2, 5, and 10 days, the wounds were inspected and photographed, and then the mice were

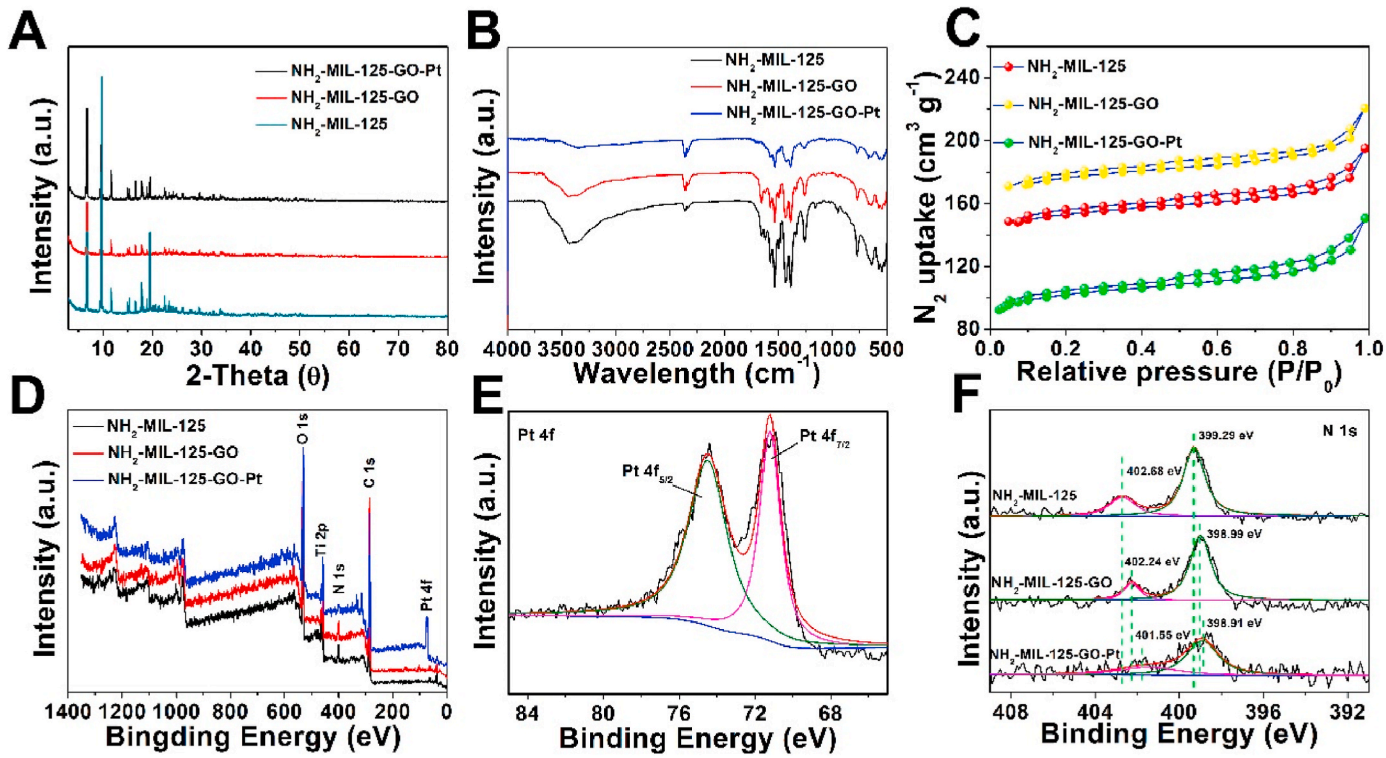

Fig. 2. The XRD (A), FTIR (B) and Nitrogen adsorption–desorption isotherms (C) of NH_2-MIL-125, NH_2-MIL-125-GO and NH_2-MIL-125-GO-Pt. (D) XPS survey spectra of NH_2-MIL-125, NH_2-MIL-125-GO and NH_2-MIL-125-GO-Pt. (E) High-resolution spectra of Pt 4f obtained from NH_2-MIL-125-GO-Pt. (F) High-resolution spectra of N 1s obtained from NH_2-MIL-125, NH_2-MIL-125-GO and NH_2-MIL-125-GO-Pt.

sacrificed. Three rats in each group were sacrificed each time for routine blood examination. At the same time, the wound surface and surrounding skin were taken, and Giemsa and hematoxylin and eosin (H&E) staining was performed on the wound on the second day, and the wounds on the fifth and tenth days were stained with H&E, respectively. These two staining methods were used to evaluate the adhesion around the wound. The number of bacteria and the progress of wound healing were attached. Finally, the heart, liver, spleen, lung and kidney of mice on the 10th day were taken for H&E staining to evaluate the biological toxicity of the material.

2.12. Statistics

In order to ensure the scientificity and accuracy of the experimental datas and results, the statistical significance against all the experiments data was evaluated and analyzed by a previous way.

3. Results and discussion

3.1. Characterization of the morphology and structure of the material

The synthesis of NH_2-MIL-125-GO-Pt was schematically illustrated in Fig. 1A. The field emission scanning electron microscope (FE-SEM) images showed that the morphology of NH_2-MIL-125 was a round cake with an average diameter of about 500 nm and a thickness of about 300 nm (Fig. S1A). The doping of lamellar GO and Pt nanoparticles did not affect the morphology of NH_2-MIL-125 (Figs. S1B and S1C). The transmission electron microscope (TEM) pictures showed that the NH_2-MIL-125 nanoparticles were tightly combined with GO (Fig. 1B), and ultra-small Pt nanoparticles were uniformly dispersed on the surface and inside of NH_2-MIL-125. The corresponding high-magnification transmission electron microscopy (HRTEM) image showed that the Pt nanoparticles were about 2–3 nm in size and showed clear lattice fringes (Fig. 1C). The lattice spacing of 0.23 nm was consistent with the d-spacing value of the (111) plane of Pt nanoparticles [19]. The pore distribution curve of the material showed that NH_2-MIL-125 had suitable micropores (3.8 nm), so both the surface and the pores of NH_2-MIL-125 could be used to support Pt nanoparticles (Fig. 1D). TEM element mapping of NH_2-MIL-125-GO-Pt showed that elements C and O were evenly distributed in GO and NH_2-MIL-125, indicating the close bonding between GO and NH_2-MIL-125 (Fig. 1E). However, elements Ti, N and Pt were mainly distributed in the same particle, which also proved that Pt was mainly distributed in NH_2-MIL-125.

X-ray diffraction (XRD) studies indicated that the diffraction peaks at 6.8, 9.8 and 11.7° could be attributed to the (101), (002), and (211) crystal planes of NH_2-MIL-125 (Fig. 2A) [20]. After loading GO and Pt nanoparticles, no new peaks of GO and Pt appeared, which might be due to the low doping content of GO and Pt. In the Fourier transform infrared spectroscopy (FTIR) spectrum of NH_2-MIL-125, the double peaks at 3456 and 3374 cm^{-1} were attributed to the symmetric and asymmetric stretching vibrations of $-NH_2$ (Fig. 2B) [21]. The peaks at 1656 and 1434 cm^{-1} were attributed to the asymmetric and symmetric tensile vibration of –O-C═O [22]. The peak of 1624 cm^{-1} was attributed to the associated bending vibration of the N–H band [23]. After doping GO, in the spectrum of NH_2-MIL-125-GO, the peak signal at 1656 cm^{-1} increased, while the peak intensity signal at 1624 cm^{-1} weakened, indicating the successful doping of GO. After further loading of Pt nanoparticles, the characteristic peak intensity of $-NH_2$ in NH_2-MIL-125-GO-Pt became very low, possibly because Pt ion was first combined with the $-NH_2$ in NH_2-MIL-125 and then further reduced to Pt nanoparticles. This also demonstrated the successful attachment of Pt nanoparticles to NH_2-MIL-125. The Brunauer-Emmett-Teller (BET) surface areas of these samples were calculated from the N_2 adsorption isotherms (Fig. 2C). The order of BET surface area was NH_2-MIL-125-GO (513.107 m^2/g) > NH_2-MIL-125 (457.19 m^2/g) > NH_2-MIL-125-GO-Pt (315.61 m^2/g). It could be found that the specific surface area of NH_2-MIL-125-GO was higher than that of NH_2-MIL-125. This might be because the addition of GO affects the crystallinity of NH_2-MIL-125.

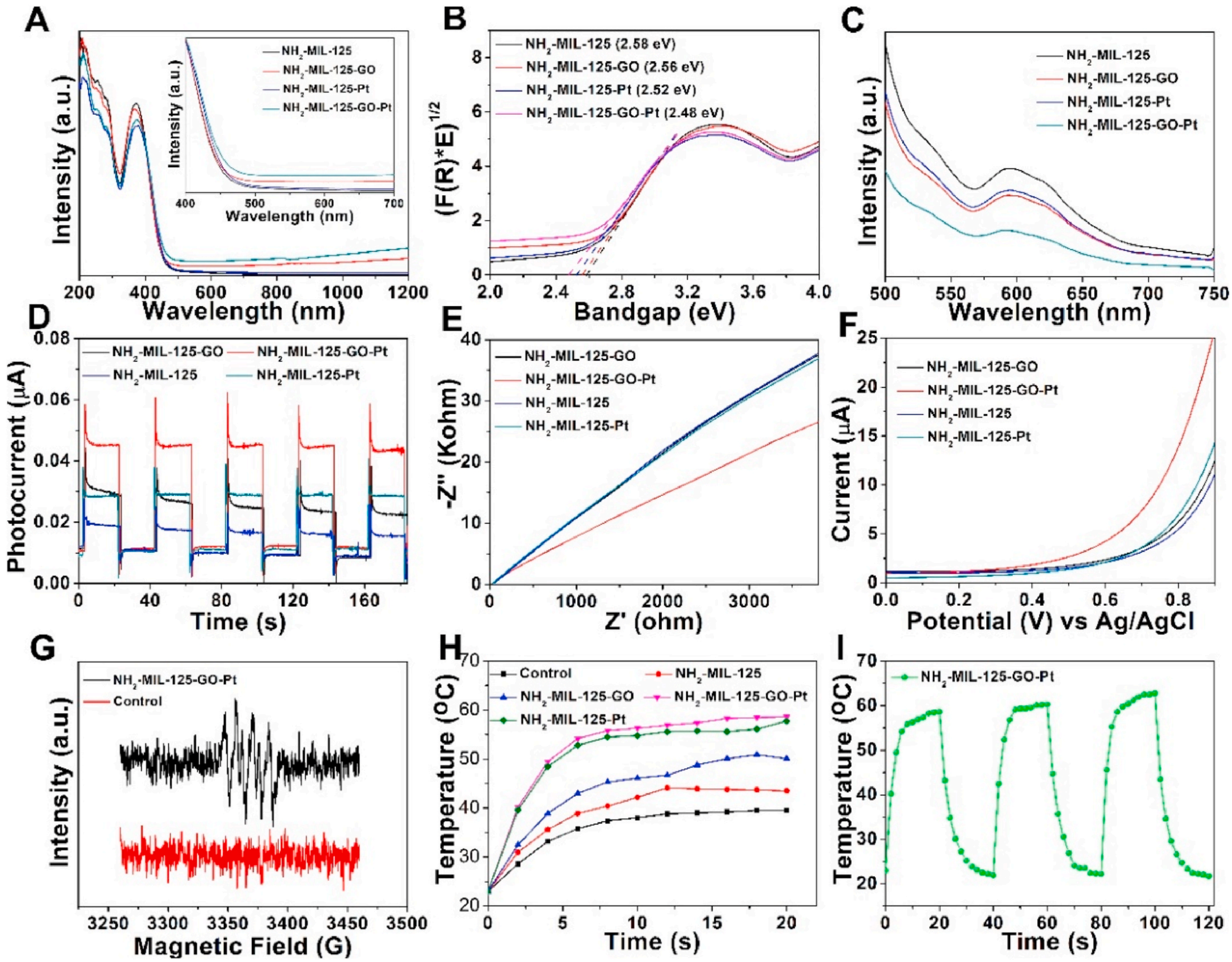

Fig. 3. Photoelectrochemical properties of NH_2-MIL-125, NH_2-MIL-125-GO, NH_2-MIL-125-Pt and NH_2-MIL-125-GO-Pt. (A) UV–vis–NIR diffuse reflectance spectra (DRS). (B) The corresponding Kubelka−Munk function plots derived from DRS. (C) PL spectra. (D) Photocurrent responses. (E) EIS spectra. (F) LSV spectra of the samples under the white light irradiation. (G) The ESR spectra of $\cdot O_2^-$. (H) The photothermal heating curves of samples. (I) Photothermal cycle curve of the NH_2-MIL-125-GO-Pt.

After loading Pt nanoparticles, the active sites on the surface of NH_2-MIL-125-GO were occupied, resulting in a decrease in the specific surface area of NH_2-MIL-125-GO-Pt. All in all, the large specific surface area of NH_2-MIL-125-GO-Pt were conducive to the progress of the catalytic reaction. The chemical composition of samples were studied by X-ray photoelectron spectroscopy (XPS). The peak signal of C of NH_2-MIL-125-GO in the wide-scan XPS spectra was stronger than that of NH_2-MIL-125, which proved the successful doping of GO (Fig. 2D) [24–26]. And the spectrum of NH_2-MIL-125-GO-Pt showed a Pt signal peak, which indicated the successful loading of Pt. Further high-resolution Pt 4f XPS analysis showed that Pt 7/2 at 71.2 eV and Pt 5/2 at 74.5 eV, indicating that Pt NPs mainly contained zero-valent Pt (Fig. 2E) [27]. In the N 1s spectrum, for NH_2-MIL-125, the binding energies at 399.29 eV and 402.68 eV were the peaks of $–NH_2$ and the positively charged N group (-N = $^+$ and $–NH-^+$), respectively (Fig. 2F) [28]. The N peak of NH_2-MIL-125-GO shifted to the low binding energy direction, which indicated that electron transfer occurred between GO and NH_2-MIL-125 [29]. Meanwhile, the signal peak of $–NH_2$ in the NH_2-MIL-125-GO-Pt further weakened, the signal peak of $–NH–^+$ almost disappeared, and the peak of N further moved towards the direction of low binding energy. The movement indicated that Pt nanoparticles were interacting with $–NH_2$, and there was electron transfer between Pt and NH_2-MIL-125-GO. In the Ti 2p and O 1s spectra (Figs. S2A and S2B), when GO and Pt were doped, both the Ti peaks and the Ti–O peaks in NH_2-MIL-125-GO and NH_2-MIL-125-GO-Pt moved towards the direction of low binding energy. This negative shift also indicated the electron transfer phenomenon between GO, Pt and NH_2-MIL-125 [30]. The C 1s spectra of the samples were similar (Fig. S2C)

3.2. Photocatalytic and photothermal properties

The UV–vis–NIR diffuse reflectance spectra (DRS) of NH_2-MIL-125 showed that its visible light absorption capacity was weak (Fig. 3A). When GO and Pt nanoparticles were loaded, the absorption band of NH_2-MIL-125-GO-Pt was red-shifted and its absorption of long wavelengths was significantly enhanced. Strong visible light absorption meant that NH_2-MIL-125-GO-Pt had stronger photon absorption capacity. In addition, the forbidden bandwidth of the material was calculated by plotting the conversion value of the Kubelka-Munk function and the photon energy (eV) [31]. The band gaps of NH_2-MIL-125, NH_2-MIL-125-GO, NH_2-MIL-125-Pt and NH_2-MIL-125-GO-Pt were estimated to be 2.58, 2.56, 2.52 and 2.48 eV, respectively (Fig. 3B). The band gap of

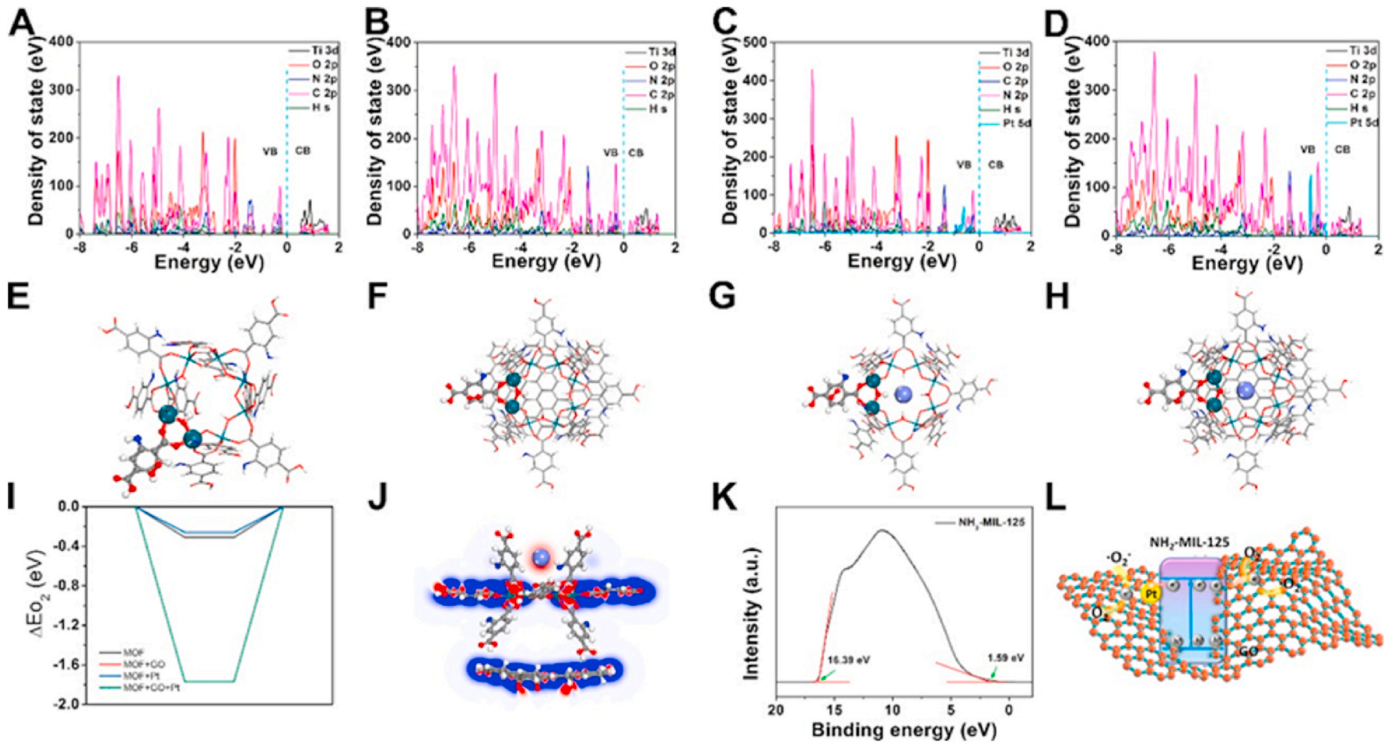

Fig. 4. The calculated DOS of (A) NH_2-MIL-125, (B) NH_2-MIL-125-GO, (C) NH_2-MIL-125-Pt and (D) NH_2-MIL-125-GO-Pt. The crystal structure after O_2 absorption on (E) NH_2-MIL-125, (F) NH_2-MIL-125-GO, (G) NH_2-MIL-125-Pt and (H) NH_2-MIL-125-GO-Pt. Red atoms indicate O atoms. (I) Adsorption energy of O_2 on the surfaces of NH_2-MIL-125, NH_2-MIL-125-GO, NH_2-MIL-125-Pt, and NH_2-MIL-125-GO-Pt crystal structure. (J) 2D charge density difference of NH_2-MIL-125-GO-Pt heterojunction. (K) Ultraviolet photoelectron spectroscopy (UPS) spectra of NH_2-MIL-125. (L) The mechanism of ROS enhancement based on the DFT calculation and UPS spectroscopy.

NH_2-MIL-125-GO-Pt was the smallest, which indicated that NH_2-MIL-125-GO-Pt was more easily photoexcited than other samples. The separation efficiency of photogenerated electron-hole pair also affects the photocatalytic performance of the material. Photoluminescence (PL) spectroscopy is used to evaluate the separation efficiency of photogenerated electron-hole pairs in materials [32]. Compared with pure NH_2-MIL-125, NH_2-MIL-125-GO-Pt had the lowest PL intensity, which meant that the addition of GO and Pt nanoparticles effectively inhibited the recombination of high charges (Fig. 3C). So NH_2-MIL-125-GO-Pt had the highest photocatalytic efficiency. In addition, the transient photocurrent response, electrochemical impedance spectroscopy (EIS) and linear sweep voltammetry (LSV) further confirmed the improvement of the interface charge separation efficiency of the NH_2-MIL-125-GO-Pt composite. The photocurrent response value showed a trend of NH_2-MIL-125-GO-Pt > NH_2-MIL-125-Pt > NH_2-MIL-125-GO > NH_2-MIL-125 (Fig. 3D). The larger the photocurrent, the higher the separation efficiency of photogenerated electron-hole pairs in the sample [33]. Therefore, the photocurrent data showed that NH_2-MIL-125-GO-Pt had the best photocatalytic effect. The EIS and LSV data showed that the NH_2-MIL-125-GO-Pt composite catalyst exhibited the fast electron transfer and high charge separation rate (Fig. 3E and F). The result showed that the doping of GO and Pt enhanced the photocatalytic efficiency of the heterojunction.

The above tests showed that NH_2-MIL-125-GO-Pt composite material had the best photocatalytic effect. Generally speaking, photogenerated electron-hole pairs will react with surrounding oxygen or water to produce ROS, which is a strong oxidant with extremely strong bactericidal ability. Electron spin resonance (ESR) spectroscopy showed that $\cdot O_2^-$ could be produced by NH_2-MIL-125-GO-Pt during irradiation (Fig. 3G) [11]. The generation of $\cdot O_2^-$ indicated that NH_2-MIL-125-GO-Pt had the possibility of acting as an antibacterial agent. Besides, NH_2-MIL-125-GO-Pt showed a good photothermal effect. After the sample was irradiated with a 300 W xenon lamp for 6 min (0.4 W/cm^2). The surface temperature of control, NH_2-MIL-125, NH_2-MIL-125-GO and NH_2-MIL-125-Pt increased to 35.8, 38.9, 43 and 52.8 °C, respectively (Fig. 3H and Fig. S3). In contrast, the temperature of NH_2-MIL-125-GO-Pt increased to 54.2 °C. The laser switching cycle experiment showed that NH_2-MIL-125-GO-Pt had good photothermal stability (Fig. 3I).

The photocatalytic mechanism of NH_2-MIL-125-GO-Pt was further study by DFT theoretical calculations. The density of electronic states (DOS) of NH_2-MIL-125 showed that the VB and CB of NH_2-MIL-125 were mainly derived from the 2p states of C, N, and O atoms in organic ligands in NH_2-MIL-125 (Fig. 4A) [34]. The 3d states of Ti atoms in NH_2-MIL-125 also partially contribute to the CB of NH_2-MIL-125, indicating that organic ligands contributed to both CB and VB of the material, while metal ions only contributed to CB. However, compared with NH_2-MIL-125, the 2p states of C and O atoms contributed significantly to CB and VB of the material in NH_2-MIL-125-GO, and more Fermi level hybridization was observed, suggesting that GO promotes electron transfer in NH_2-MIL-125 (Fig. 4B) [35]. The introduction of Pt mainly contributed to the VB of NH_2-MIL-125, indicating that the Pt nanoparticles may mainly interact with the organic ligands of NH_2-MIL-125 (Fig. 4C). More importantly, the introduction of Pt energy levels could reduce the energy required for electron transition, which was conducive to the separation and transfer of electrons [36]. Therefore, the introduction of Pt nanoparticles also promoted the electron transfer of NH_2-MIL-125. After the simultaneous introduction of Pt and GO, the Fermi level hybridization in NH_2-MIL-125 was more, indicating that the introduction of Pt and GO simultaneously increases the electron transfer in NH_2-MIL-125. Since O_2 is an important factor for the photocatalytic production of $\cdot O_2^-$, we calculated the material's ability to adsorb O_2 and the location of O_2. As shown in Fig. 4E–H, O_2 molecules were all adsorbed on the organic ligands of NH_2-MIL-125. The energy absorption

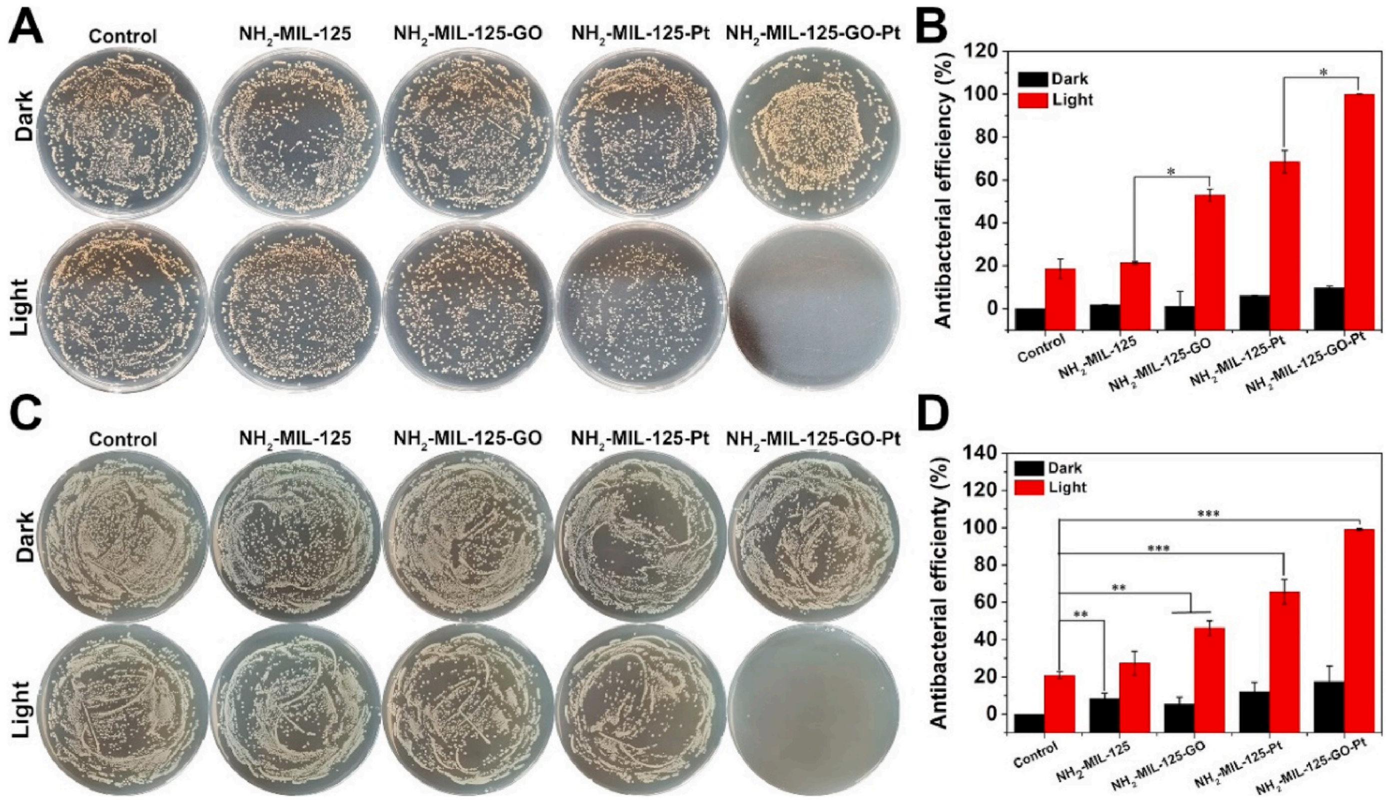

Fig. 5. (A) Spread plate results of *S. aureus* eradication in different samples after treatment in the dark or irradiation with white light for 20 min and (B) The corresponding antibacterial ratio of different samples. (C) Spread plate results of *E. coli* eradication in different samples after treatment in the dark or irradiation with white light for 20 min and (D) The corresponding antibacterial ratio of different samples. (n = 3, means ± SD). *$p < 0.05$, **$p < 0.01$, ***$p < 0.001$.

of the sample was NH_2-MIL-125-GO-Pt < NH_2-MIL-125 < NH_2-MIL-125-GO = NH_2-MIL-125-Pt, indicating that the NH_2-MIL-125-GO-Pt heterojunction had a strong oxygen absorption capacity. The charge density difference of NH_2-MIL-125-GO-Pt was shown in Fig. 4J, and electron accumulation (red area) and depletion (blue area) reveal the charge distribution state of the whole system. There was electron accumulation between Pt nanoparticles and MOF, the surface of Pt nanoparticles was negatively charged, while MOF and GO were in a state of loss of electrons and were positively charged, indicating that a built-in electric field could be formed between Pt, MOF and GO, which was beneficial to the separation of electron-hole pairs for the entire system [37,38]. The work function (Φ) was calculated using ultraviolet photoelectron spectroscopy (UPS) spectroscopy (Fig. 4K) [39]. The Φ of NH_2-MIL-125 was 4.81 eV, and the energy difference between VB and Φ was 1.59 eV. Therefore, VB and CB were about 1.9 eV and −0.68 eV, respectively (compared to NHE). Based on DFT computation and UPS, the ROS enhancement mechanism was shown in Fig. 4L. Since the VB and CB of NH_2-MIL-125 were 1.9 and −0.68 eV, respectively, and the potential of O_2 to become $\cdot O_2^-$ was −0.33 eV (compared to NHE), the value of CB of NH_2-MIL-125 was less than this potential, so NH_2-MIL-125 could produce $\cdot O_2^-$. When the NH_2-MIL-125-GO-Pt heterojunction was irradiated with light, the electrons on the VB of NH_2-MIL-125 were excited to migrate to its CB, and then the electrons on the CB had two migration paths. One of them was to transfer to the Pt nanoparticles through the Schottky junction, and then the electrons on the Pt nanoparticles reacted with O_2 to generate $\cdot O_2^-$. Another migration path was to transfer to GO and reacted with O_2 to generate $\cdot O_2^-$. Therefore, the NH_2-MIL-125-GO-Pt heterojunction could effectively generate $\cdot O_2^-$ under illumination.

3.3. Antibacterial activity in vitro

The plate coating method was used to determine the antibacterial efficiency of the material against *S. aureus* and *E. coli*. The control, NH_2-MIL-125, and NH_2-MIL-125-GO groups showed almost the same bacterial colonies after being cultured in the dark for 20 min (Fig. 5A and C). However, the number of colonies in the NH_2-MIL-125-Pt and NH_2-MIL-125-GO-Pt groups after 20 min of incubation in the dark was slightly less than that of the control group (the *S. aureus* colonies reduced 6.14%, 9.71% and the *E. coli* reduced 12.09%, 17.44% in Fig. 5B and D). These results indicated that the impact of the sample on *S. aureus* and *E. coli* was negligible under dark conditions. In contrast, after 20 min of exposure to the light, the bacteria in the control group were slightly reduced, and its antibacterial rate against *S. aureus* and *E. coli* was about 18.62% and 20.83%, respectively. This was because the UV light in the xenon lamp would kill some bacteria. In contrast, the bacterial colony groups on the NH_2-MIL-125, NH_2-MIL-125-GO, NH_2-MIL-125-Pt and NH_2-MIL-125-GO-Pt groups showed different degrees of decline. The antibacterial efficacy of samples against to *S. aureus* was 21.36%, 52.95%, 68.44%, and 99.94%, respectively. Similarly, the antibacterial effects of the samples against *E. coli* were 27.37%, 46.22%, 65.58% and 99.12%, respectively. These results indicated that the combination of the highest photocatalytic efficiency and suitable photothermal had a much higher antibacterial effect on *S. aureus* and *E. coli*.

The antibacterial mechanism of the materials was further explored. FE-SEM pictures showed that the *S. aureus* and *E. coli* cultured with the control group, NH_2-MIL-125 and NH_2-MIL-125-GO groups showed normal and intact morphology under dark conditions, indicating that these three groups had no obvious antibacterial properties without light exposure (Fig. 6A and B). The surface of the bacteria in the NH_2-MIL-125-Pt and NH_2-MIL-125-GO-Pt groups was slightly wrinkled, indicating that the two groups had a little antibacterial effect under dark condition.

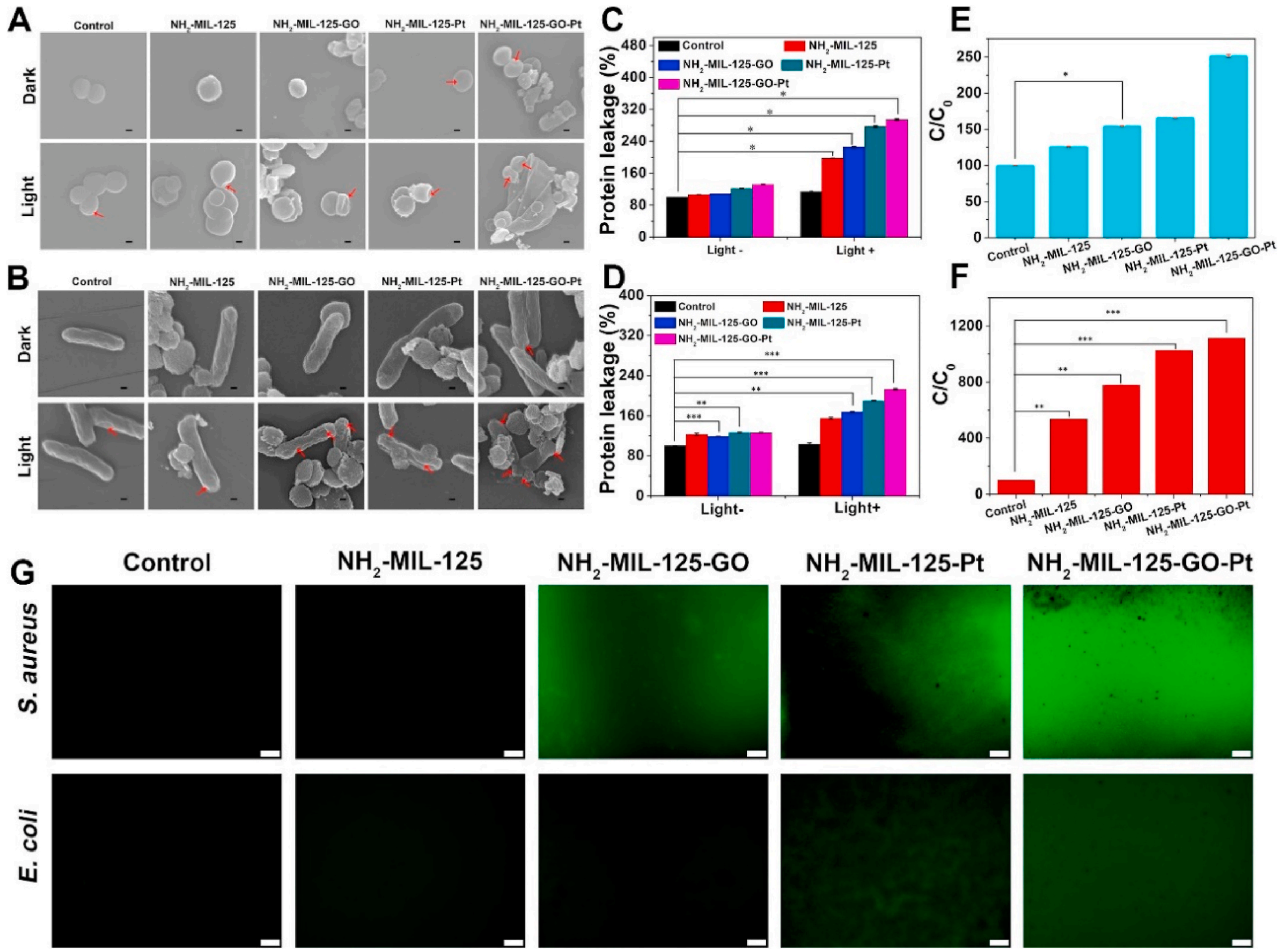

Fig. 6. FE-SEM images of the morphology of *S. aureus* (A) and *E. coli* (B) treated with or without light irradiation. The relative protein leakage concentration for the *S. aureus* (C) and *E. coli* (D) treated or not treated with white light irradiation. The ONPG hydrolysis assay of *S. aureus* (E) and *E. coli* (F) treated with white light irradiation. (G) Fluorescence staining images of *S. aureus* and *E. coli* treated by materials with DCFH-DA probe. The error bars (n = 3) represent means ± SD. *$p < 0.05$, **$p < 0.01$, ***$p < 0.001$.

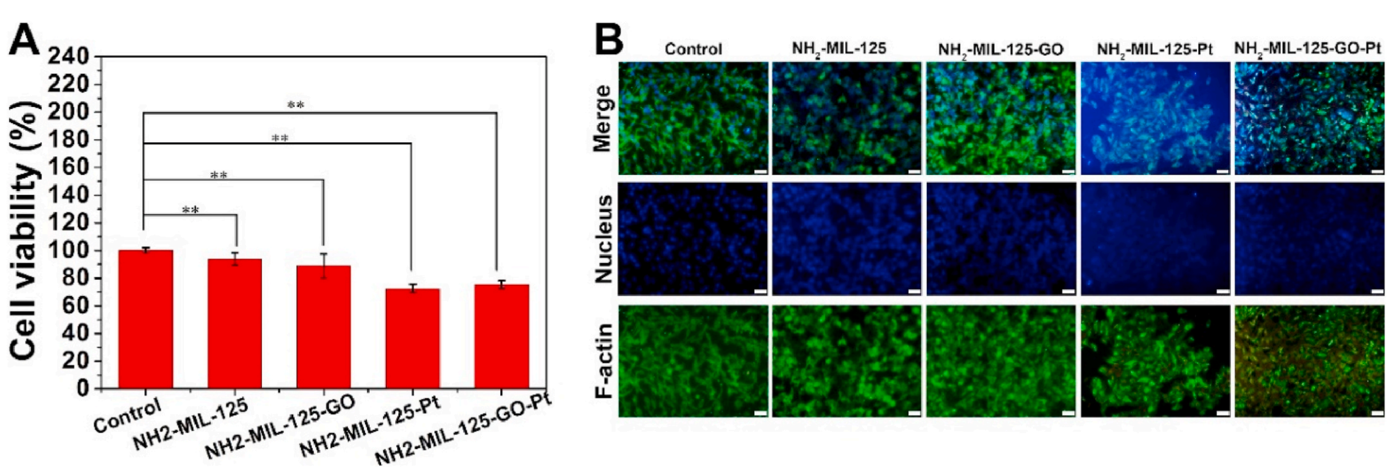

Fig. 7. (A) Cytotoxicity of NH_2-MIL-125, NH_2-MIL-125-GO, NH_2-MIL-125-Pt and NH_2-MIL-125-GO-Pt after co-culturing for 1 d with NIH3T3 cells with various concentrations. The error bars indicate means ± SD (n = 3). (B) Fluorescence staining of control, NH_2-MIL-125, NH_2-MIL-125-GO, NH_2-MIL-125-Pt and NH_2-MIL-125-GO-Pt. Scale bars are 50 μm.

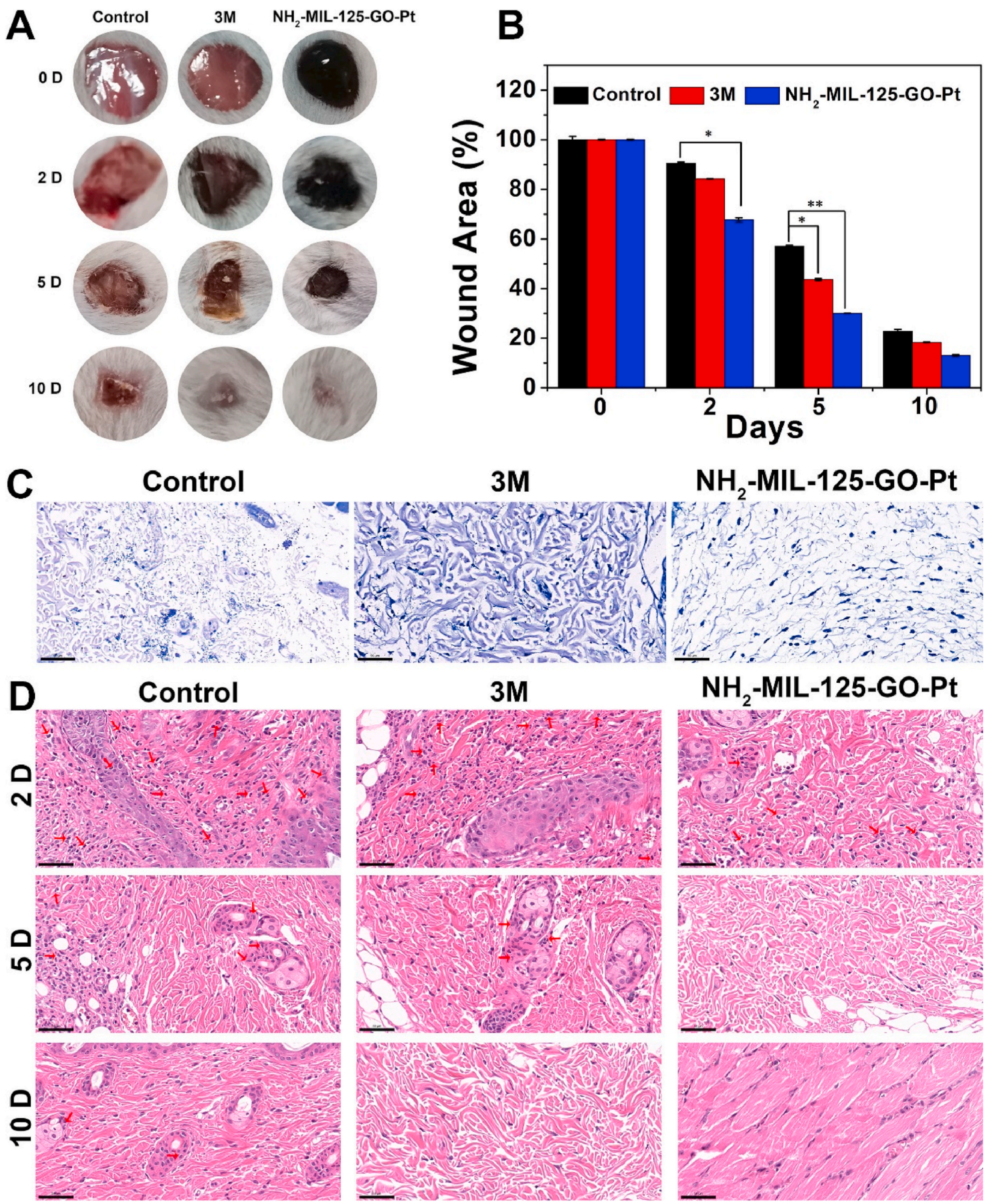

Fig. 8. (A) Images of wound size at 0, 2, 5, and 10 days after treated with control group, 3 M dressing group, and NH_2-MIL-125-GO-Pt group with white light irradiation. (B) The corresponding change in wound area calculated from wound images. (C) Giemsa stained images showing the extent of infection in the wound area after 2 days of treatment. Scale bar is 50 μm. (D) H&E stained images showing the extent of infection in skin tissue after 2, 5, 10 days. Scale bar is 50 μm. Error bars represent mean ± SD: $^*P < 0.05$, $^{**}P < 0.01$.

In contrast, the bacterial membranes of *S. aureus* and *E. coli* in all groups became distorted after irradiation. The above phenomenon showed that light could excite the material to kill bacteria by destroying the bacterial membrane in a short time. When the bacterial membrane was damaged, proteins would leak out. The protein leakage of *S. aureus* and *E. coli* co-cultured with the materials increased gradually with the improvement of photothermal and photocatalytic effect of the materials after illumination, and the protein leakage of NH_2-MIL-125-GO-Pt group was the largest (Fig. 6C and D). The o-nitrophenyl-β-galactoside (ONPG) hydrolysis test could be used to evaluate changes in cell membrane permeability [35]. Experimental data showed that the ONPG value of the NH_2-MIL-125-GO-Pt group was the highest for both the *S. aureus* and the *E. coli*, indicating that the bacterial membrane permeability of NH_2-MIL-125-GO-Pt increased and the antibacterial effect was the best under the synergistic effect of photothermal and photocatalytic (Fig. 6E and F). In addition, DCFH-DA was used to evaluate the ROS inside the bacteria after antibacterial experiments (Fig. 6G). The NH_2-MIL-125--GO-Pt group showed the brightest green fluorescence, regardless of whether the material was co-cultured with *S. aureus* or *E. coli* after 20 min of irradiation, indicating that the NH_2-MIL-125-GO-Pt group had the largest intracellular ROS production. In fact, too much ROS in bacteria can cause bacterial physiological disorder, resulting in bacterial death [35]. Therefore, the DCFH-DA data show that the NH_2-MIL-125-GO-Pt group has the most excellent antibacterial rate under the synergy of photocatalysis and photothermal.

3.4. *In vitro cell experiment*

The biological toxicity of the sample was evaluated by the 3-[4, 5-dimethylthiazol-2-yl]-2, 5-diphenyltetrazolium bromide (MTT) and cytofluorescence methods [40]. The cell viability of the NH_2-MIL-125-GO-Pt group was 75.34% compared with the control group, indicating that the cytotoxicity of NH_2-MIL-125-GO-Pt was weaker (Fig. 7A). Fluorescence experiments showed that compared with the control group, the cells in the material group showed normal morphology, with complete cytoplasmic spreading and filopodia extension, indicating that these materials had no obvious cytotoxicity (Fig. 7B).

3.5. *In vivo animal experiment*

A mouse wound model was further constructed to assess whether the material could promote wound healing. The wound closure diagrams at different time points showed that the wounds in the NH_2-MIL-125-GO-Pt group were basically healed after 10 days of treatment, while the wounds in the other groups still had obvious defects (Fig. 8A). The corresponding change trend chart of wound area showed that the wounds in the NH_2-MIL-125-GO-Pt group were always smaller than those in the other groups (Fig. 8B). During the experiment, all groups showed significant bacterial infection after 2 days of treatment. The number of attached bacteria around the wound could be observed by Giemsa staining (Fig. 8C). It could be seen that there were a large number of bacteria in the control group, and the bacteria in the 3M group were significantly less than those in the control group. The number of bacteria in the NH_2-MIL-125-GO-Pt group was significantly reduced. The number of neutrophils in soft tissue also indicated bacterial infection, as neutrophils rapidly migrate from circulating blood to the site of infection in response to infection [41]. As shown in Fig. 8D, many lobulated neutrophil staining could be observed around the wound marked by the red arrow after hematoxylin and eosin (H&E) staining, indicating severe bacterial infection, especially in the control and 3M groups on the first 2 days. In contrast, the number of neutrophils in the NH_2-MIL-125-GO-Pt group was lower, and most cells were normal, indicating a relatively small infection, indicating a significant in vivo bactericidal effect of NH_2-MIL-125-GO-Pt.

In vivo microscopic therapeutic efficacy was determined by blood routine analysis, as shown in Fig. S4. The parameters tested in the treatment groups, white blood cells (WBC) (Fig. S4A) and neutrophils (Fig. S4B), were within normal ranges, indicating that NH_2-MIL-125-GO-Pt had significant *in vivo* antibacterial properties. Furthermore, histological analysis of major organs (heart, liver, spleen, lung, and kidney) did not reveal any abnormal effects or damage after 10 days of treatment (Fig. S4C), suggesting that NH_2-MIL-125-GO-Pt was a biosafety material.

4. Conclusion

In this work, the NH_2-MIL-125-GO-Pt ternary heterojunction was designed and prepared by simple hydrothermal process followed by *in situ* reduction process. The doping of GO and Pt can effectively promote the interface contact between NH_2-MIL-125-GO-Pt components and narrow the band gap between them, which can effectively improve the separation and transfer of photogenic carriers generated by NH_2-MIL-125, thus improving the photocatalytic efficiency of NH_2-MIL-125, and thus improving the generation of ROS. The composite not only has excellent photocatalytic effect, but also has good photothermal effect. Therefore, NH_2-MIL-125-GO-Pt composite material has the potential as a fungicide. The *in vitro* antibacterial results showed that the antibacterial rate of the composite material against *S. aureus* and *E. coli* was as high as 99.94% and 99.12%, respectively, after 20 min of white light irradiation. We believe that this work can provide more perspectives in the field of antimicrobial therapy.

Declaration of competing interest

The authors declare that they have no competing interests.

Acknowledgements

This work is jointly supported by the China National Funds for Distinguished Young Scientists (No.51925104), and the National Natural Science Foundation of China (Nos. 51871162, and 52173251).

Appendix A. Supplementary data

Supplementary data to this article can be found online at https://doi.org/10.1016/j.bioactmat.2022.03.035.

References

[1] J. Liu, D. Wu, N. Zhu, Y. Wu, G. Li, Antibacterial mechanisms and applications of metal-organic frameworks and their derived nanomaterials, Trends Food Sci. Technol. 109 (2021) 413–434.
[2] R. Das, C.D. Vecitis, A. Schulze, B. Cao, A.F. Ismail, X. Lu, J. Chen, S. Ramakrishna, Recent advances in nanomaterials for water protection and monitoring, Chem. Soc. Rev. 46 (22) (2017) 6946–7020.
[3] A. Gupta, S. Mumtaz, C.-H. Li, I. Hussain, V.M. Rotello, Combatting antibiotic-resistant bacteria using nanomaterials, Chem. Soc. Rev. 48 (2) (2019) 415–427.
[4] Y. Wang, Y. Yang, Y. Shi, H. Song, C. Yu, Antibiotic-free antibacterial strategies enabled by nanomaterials: progress and perspectives, Adv. Mater. 32 (18) (2020) 1904106.
[5] Z. Cao, Y. Luo, Z. Li, L. Tan, X. Liu, C. Li, Y. Zheng, Z. Cui, K.W.K. Yeung, Y. Liang, S. Zhu, S. Wu, Antibacterial hybrid hydrogels, Macromol. Biosci. 21 (1) (2020) 2000252.
[6] J. Huo, Q. Jia, H. Huang, J. Zhang, P. Li, X. Dong, W. Huang, Emerging photothermal-derived multimodal synergistic therapy in combating bacterial infections, Chem. Soc. Rev. 50 (15) (2021) 8762–8789.
[7] R. Yang, G. Song, L. Wang, Z. Yang, J. Zhang, X. Zhang, S. Wang, L. Ding, N. Ren, A. Wang, X. Yu, Full solar-spectrum-driven antibacterial therapy over hierarchical Sn_3O_4/PDINH with enhanced photocatalytic activity, Small 17 (39) (2021) 2102744.
[8] M. Yang, S. Qiu, E. Coy, S. Li, K. Załęski, Y. Zhang, H. Pan, G. Wang, NIR-responsive TiO_2 biometasurfaces: toward in situ photodynamic antibacterial therapy for biomedical implants, Adv. Mater. 34 (6) (2022) 2106314.
[9] R. Lv, Y.-Q. Liang, Z.-Y. Li, S.-L. Zhu, Z.-D. Cui, S.-L. Wu, Flower-like CuS/graphene oxide with photothermal and enhanced photocatalytic effect for rapid bacteria-killing using visible light, Rare Met. 41 (2) (2022) 639–649.
[10] D.-L. Han, P.-L. Yu, X.-M. Liu, Y.-D. Xu, S.-L. Wu, Polydopamine modified CuS@HKUST for rapid sterilization through enhanced photothermal property and photocatalytic ability, Rare Met. 41 (2) (2022) 663–672.
[11] L. Hong, X. Liu, L. Tan, Z. Cui, X. Yang, Y. Liang, Z. Li, S. Zhu, Y. Zheng, K.W. K. Yeung, D. Jing, D. Zheng, X. Wang, S. Wu, Rapid biofilm elimination on bone implants using near-infrared-activated inorganic semiconductor heterostructures, Adv. Healthc. Mater. 8 (19) (2019) 1900835.
[12] X. Miao, F. Yu, K. Liu, Z. Lv, J. Deng, T. Wu, X. Cheng, W. Zhang, X. Cheng, X. Wang, High special surface area and "warm light" responsive ZnO: synthesis mechanism, application and optimization, Bioact. Mater. 7 (2022) 181–191.
[13] Q. Zheng, X. Liu, Y. Zheng, K.W.K. Yeung, Z. Cui, Y. Liang, Z. Li, S. Zhu, X. Wang, S. Wu, The recent progress on metal–organic frameworks for phototherapy, Chem. Soc. Rev. 50 (8) (2021) 5086–5125.
[14] Y. Luo, X. Liu, L. Tan, Z. Li, K.W.K. Yeung, Y. Zheng, Z. Cui, Y. Liang, S. Zhu, C. Li, X. Wang, S. Wu, Enhanced photocatalytic and photothermal properties of ecofriendly metalorganic framework heterojunction for rapid sterilization, Chem. Eng. J. 405 (2021) 126730.
[15] Y. Luo, J. Li, X. Liu, L. Tan, Z. Cui, X. Feng, X. Yang, Y. Liang, Z. Li, S. Zhu, Y. Zheng, K.W.K. Yeung, Cao Yang, X. Wang, S. Wu, Dual metal-organic framework heterointerface, ACS Cent. Sci. 5 (9) (2019) 1591–1601.
[16] J. Ran, J. Qu, H. Zhang, T. Wen, H. Wang, S. Chen, L. Song, X. Zhang, L. Jing, R. Zheng, S.-Z. Qiao, 2D metal organic framework nanosheet: a universal platform

promoting highly efficient visible-light-induced hydrogen production, Adv. Energy Mater. 9 (11) (2019) 1803402.
[17] M. Xu, D. Li, K. Sun, L. Jiao, C. Xie, C. Ding, H.-L. Jiang, Interfacial microenvironment modulation boosting electron transfer between metal nanoparticles and MOFs for enhanced photocatalysis, Angew. Chem. Int. Ed. 60 (30) (2021) 16327–16376.
[18] F. Guo, Y.-P. Wei, S.-Q. Wang, X.-Y. Zhang, F.-M. Wang, W.-Y. Sun, Pt nanoparticles embedded in flowerlike NH_2-UiO-68 for enhanced photocatalytic carbon dioxide reduction, J. Mater. Chem. 7 (46) (2019) 26490–26495.
[19] Z. Zheng, H. Xu, Z. Xu, J. Ge, A monodispersed spherical Zr-based metal-organic framework catalyst, Pt/Au@Pd@UIO-66, comprising an Au@Pd core-shell encapsulated in a UIO-66 center and its highly selective CO_2 hydrogenation to produce CO, Small 14 (5) (2018) 1702812.
[20] H. Li, X. Liu, H. Feng, J. Zhao, P. Lu, M. Fu, W. Guo, Y. Zhao, Y. He, NH_2-MIL-125 (Ti) with transient metal centers via novel electron transfer routes for enhancing photocatalytic NO removal and H_2 evolution, Catal. Sci. Technol. 11 (18) (2021) 6225–6233.
[21] J. Cai, J.-Y. Lu, Q.-Y. Chen, L.-L. Qu, Y.-Q. Lu, G.-F. Gao, Eu-based MOF/graphene oxide composite: a novel photocatalyst for the oxidation of benzyl alcohol using water as oxygen source, New J. Chem. 41 (10) (2017) 3882–3886.
[22] G. Zhou, M.-F. Wu, Q.-J. Xing, F. Li, H. Liu, X.-B. Luo, J.-P. Zou, J.-M. Luo, A.-Q. Zhang, Synthesis and characterizations of metal-free semiconductor/MOFs with good stability and high photocatalytic activity for H_2 evolution: a novel Z-Scheme heterostructured photocatalyst formed by covalent bonds, Appl. Catal. B Environ. 220 (2018) 607–614.
[23] N.M. Mahmoodi, A. Taghizadeh, M. Taghizadeh, J. Abdi, In situ deposition of Ag/AgCl on the surface of magnetic metal-organic framework nanocomposite and its application for the visible-light photocatalytic degradation of Rhodamine dye, J. Hazard Mater. 378 (2019) 120741.
[24] M. Sun, J. Li, Graphene oxide membranes: functional structures, preparation and environmental applications, Nano Today 20 (2018) 121–137.
[25] D. R. Dreyer, A. D. Todd, C. W. Bielawski, Harnessing the chemistry of graphene oxide, Chem. Soc. Rev. 43(15) 5288-5301.
[26] J. Wu, L. Jia, Y. Zhang, Y. Qu, B. Jia, D.J. Moss, Graphene oxide for integrated photonics and flat optics, Adv. Mater. 33 (3) (2021) 2006415.
[27] Z. Gao, Y. Li, Y. Zhang, K. Cheng, P. An, F. Chen, J. Chen, C. You, Q. Zhu, B. Sun, Biomimetic platinum nanozyme immobilized on 2D metal-organic frameworks for mitochondrion-targeting and oxygen self-supply photodynamic therapy, ACS Appl. Mater. Interfaces 12 (2) (2020) 1963–1972.
[28] H. Wang, X. Yuan, Y. Wu, G. Zeng, X. Chen, L. Leng, Z. Wu, L. Jiang, H. Li, Facile synthesis of amino-functionalized titanium metal-organic frameworks and their superior visible-light photocatalytic activity for Cr (VI) reduction, J. Hazard Mater. 286 (2015) 187–194.
[29] X. Zheng, Y. Li, J. Yang, S. Cui, Z-Scheme heterojunction Ag/NH_2-MIL-125(Ti)/CdS with enhanced photocatalytic activity for ketoprofen degradation: mechanism and intermediates, Chem. Eng. J. 422 (2021) 130105.
[30] S.J. Shah, R. Wang, Z. Gao, Y. Muhammad, H. Zhang, Z. Zhang, Z. Chu, Z. Zhao, Z. Zhao, IL-assisted synthesis of defect-rich polyaniline/NH_2-MIL-125 nanohybrids with strengthened interfacial contact for ultra-fast photocatalytic degradation of acetaldehyde under high humidity, Chem. Eng. J. 411 (2021) 128590.
[31] Y. Fu, K. Zhang, Y. Zhang, Y. Cong, Q. Wang, Fabrication of Visible-Light-Active MR/NH_2-MIL-125(Ti) Homojunction with Boosted Photocatalytic Performance, vol. 412, 2021, p. 128722, 15.
[32] X. Jiang, H. Gong, Q. Liu, M. Song, C. Huang, In situ construction of NiSe/$Mn_{0.5}Cd_{0.5}S$ composites for enhanced photocatalytic hydrogen production under visible light, Appl. Catal. B Environ. 268 (5) (2020) 118439.
[33] J. Li, Q. Pei, R. Wang, Y. Zhou, Z. Zhang, Q. Cao, D. Wang, W. Mi, Y. Du, Enhanced photocatalytic performance through magnetic field boosting carrier transport, ACS Nano 12 (4) (2018) 3351–3359.
[34] S. Chen, G. Hai, H. Gao, X. Chen, A. Li, X. Zhang, W. Dong, Modulation of the charge transfer behavior of Ni(II)-doped NH_2-MIL-125(Ti): regulation of Ni ions content and enhanced photocatalytic CO_2 reduction performance, Chem. Eng. J. 406 (2021) 126886.
[35] Y. Li, X. Liu, L. Tan, Z. Cui, D. Jing, X. Yang, Y. Liang, Z. Li, S. Zhu, Y. Zheng, K.W. K. Yeung, D. Zheng, X. Wang, S. Wu, Eradicating multidrug-resistant bacteria rapidly using a multi functional g-C_3N_4@Bi_2S_3 nanorod heterojunction with or without antibiotics, Adv. Funct. Mater. 29 (20) (2019) 1900946.
[36] H. Liu, H. Mei, N. Miao, L. Pan, Z. Jin, G. Zhu, J. Gao, J. Wang, L. Cheng, Synergistic photocatalytic NO removal of oxygen vacancies and metallic bismuth on $Bi_{12}TiO_{20}$ nanofibers under visible light irradiation, Chem. Eng. J. 414 (2021) 128748.
[37] Y. Zhang, J. Zhao, H. Wang, B. Xiao, W. Zhang, X. Zhao, T. Lv, M. Thangamuthu, J. Zhang, Y. Guo, J. Ma, L. Lin, J. Tang, R. Huang, Q. Liu, Single-atom Cu anchored catalysts for photocatalytic renewable H_2 production with a quantum efficiency of 56%, Nat. Commun. 13 (1) (2022) 1–10.
[38] C. Wang, Y. Luo, X. Liu, Z. Cui, Y. Zheng, Y. Liang, Z. Li, S. Zhu, J. Lei, X. Feng, S. Wu, The enhanced photocatalytic sterilization of MOF-Based nanohybrid for rapid and portable therapy of bacteria-infected open wounds, Bioact, Materials 13 (2021) 200–211.
[39] J. Li, Z. Li, X. Liu, C. Li, Y. Zheng, K.W.K. Yeung, Z. Cui, Y. Liang, S. Zhu, W. Hu, Y. Qi, T. Zhang, X. Wang, S. Wu, Interfacial engineering of $Bi_2S_3/Ti_3C_2T_x$ MXene based on work function for rapid photo-excited bacteria-killing, Nat. Commun. 12 (1) (2021) 1–10.
[40] Z.-X. Han, X.-M. Liu, L. Tan, Z.-Y. Li, Y.-F. Zheng, K.W.-K. Yeung, Z.-D. Cui, Y.-Q. Liang, S.-L. Zhu, S.-L. Wu, Photothermal-controlled sustainable degradation of protective coating modified mg alloy using near-infrared light, Rare Met. 40 (9) (2021) 2538–2551.
[41] M. Li, X. Liu, L. Tan, Z. Cui, X. Yang, Z. Li, Y. Zheng, K.W.K. Yeung, P.K. Chu, S. Wu, Noninvasive rapid bacteria-killing and acceleration of wound healing through photothermal/photodynamic/copper ion synergistic action of a hybrid hydrogel, Biomater. Sci. 6 (8) (2018) 2110–2121.